

RIT-Eyes: Rendering of near-eye images for eye-tracking applications

Nitinraj Nair

nrn2741@rit.edu

Rochester Institute of Technology
Rochester, NY, USA 14623

Zhizhuo Yang

zy8981@rit.edu

Rochester Institute of Technology
Rochester, New York, USA

Rakshit Kothari

rsk3900@rit.edu

Rochester Institute of Technology
Rochester, NY, USA

Gabriel J. Diaz

gabriel.diaz@rit.edu

Rochester Institute of Technology
Rochester, NY, USA

Reynold J. Bailey

rjb@cs.rit.edu

Rochester Institute of Technology
Rochester, NY, USA

Aayush K. Chaudhary

akc5959@rit.edu

Rochester Institute of Technology
Rochester, NY, USA

Jeff B. Pelz

jeff.pelz@cis.rit.edu

Rochester Institute of Technology
Rochester, NY, USA



Figure 1: Sample images generated using our synthetic eye image generation platform. RGB images (top). Corresponding simulated infrared images (bottom). Pixels assigned a label through the process of semantic segmentation are shown on the bottom rightmost images with and without skin (to illustrate placement of the eyeball). Red = pupil, green = iris, blue = sclera.

ABSTRACT

Deep neural networks for video-based eye tracking have demonstrated resilience to noisy environments, stray reflections, and low resolution. However, to train these networks, a large number of manually annotated images are required. To alleviate the cumbersome process of manual labeling, computer graphics rendering is employed to automatically generate a large corpus of annotated eye images under various conditions. In this work, we introduce a synthetic eye image generation platform that improves upon previous work by adding features such as an active deformable iris, an aspherical cornea, retinal retro-reflection, gaze-coordinated eye-lid deformations, and blinks. To demonstrate the utility of our

Permission to make digital or hard copies of all or part of this work for personal or classroom use is granted without fee provided that copies are not made or distributed for profit or commercial advantage and that copies bear this notice and the full citation on the first page. Copyrights for components of this work owned by others than ACM must be honored. Abstracting with credit is permitted. To copy otherwise, or republish, to post on servers or to redistribute to lists, requires prior specific permission and/or a fee. Request permissions from permissions@acm.org.

Conference'17, Washington, DC, USA

© 2016 ACM. 978-x-xxxx-xxxx-x/YY/MM...\$15.00

DOI: 10.1145/nmnnnnn.nnnnnnn

platform, we render images reflecting the represented gaze distributions inherent in two publicly available datasets, NVGaze and OpenEDS. We also report on the performance of two semantic segmentation architectures (SegNet and RITnet) trained on rendered images and tested on the original datasets.

CCS CONCEPTS

•Computing methodologies → Cross-validation; Mesh geometry models; Rendering;

KEYWORDS

eye-tracking, synthetic datasets, semantic segmentation, neural networks

ACM Reference format:

Nitinraj Nair, Rakshit Kothari, Aayush K. Chaudhary, Zhizhuo Yang, Gabriel J. Diaz, Jeff B. Pelz, and Reynold J. Bailey. 2016. RIT-Eyes: Rendering of near-eye images for eye-tracking applications. In *Proceedings of ACM Conference, Washington, DC, USA, July 2017 (Conference'17)*, 10 pages.

DOI: 10.1145/nmnnnnn.nnnnnnn

1 INTRODUCTION AND RELATED WORK

Modern video-based eye-trackers use infrared cameras to monitor movements of the eyes in order to gather information about the visual behavior and perceptual strategies of individuals engaged in various tasks. Eye-trackers have traditionally been mounted to computer screens or worn directly on the head for mobile applications and are increasingly being embedded in head-mounted-displays to support rendering and interaction in virtual and augmented reality applications. Contemporary algorithms for estimating gaze direction rely heavily on the segmentation of specific regions of interest in the eye images, such as the pupil (see Figure 1 bottom right). These features are then used to estimate the causal 3D geometry, in the form of a 3D model of the spherical eye in camera space [32]. Segmentation is complicated by the presence of corrective lenses or by reflections of the surrounding environment upon intervening physiology, such as the cornea and the tear layer. Convolutional neural networks (CNNs) have presented a promising new approach for the annotation of eye images even in these challenging conditions [14, 18, 21, 33, 36, 37]. However promising, the use of CNNs trained through supervised learning requires a large corpus of annotated eye images. Manual annotation is time-intensive and, although these datasets exist, they are susceptible to errors introduced during human annotation, and only a few exist that include manually segmented image features other than the pupil center which are necessary for building an accurate 3D model of the eye. For a comprehensive list of existing datasets, please refer to Garbin *et al.* [15]. Although existing dataset images may include reflections of the surrounding environment, their inclusion has been unsystematic, and their contributions to the robustness of segmentation remain unclear.

To alleviate these limitations, solutions proposed by Bohme *et al.* [8], Swirski *et al.* [31], Wood *et al.* [34, 35], and Kim *et al.* [18] involve rendering near-eye images in which the location of image features is known, circumventing the need for manual annotation. In this work, we present a new dataset (see example images in Figure 1), which builds on the success of our predecessors. Similar to previous efforts, we use a 3D model of the human eye to render 2D imagery similar to what is captured by an eye-tracker. Our synthetic eye image generation platform introduces several improvements including an accurate aspherical corneal model, a deformable iris, the lacrimal caruncle (the small pink nodule located at the inner corner of the eye), gaze-coordinated blinks, and a retina with retro-reflective properties which can aid in developing ‘bright pupil’ solutions [22] for head-mounted or remote eye trackers (see section 3 and Table 1 for a comprehensive list of improvements).

The real evaluation of the effectiveness of any synthetic dataset lies in its ability to be leveraged in real-world problems. Although initial efforts demonstrate that CNNs trained on artificial stimuli for semantic segmentation can generalize to true imagery [18, 26, 27], these initial tests are limited to specific applications. Kim *et al.* [18] showed that despite their best efforts to model realistic distributions of natural eye imagery in a virtual reality headset, training on synthetic eye images while testing on real data resulted in a 3.1° accuracy error on average, which is $\sim 1^\circ$ higher than training on real imagery. Park *et al.* utilized the UnityEyes dataset [34] to train a stacked hourglass architecture [23] to detect landmarks in

	Unity Eyes	Synth Eyes	NVGaze	Swirski	Ours
Aspherical cornea	×	×	×	×	✓
Retroreflection	×	×	×	×	✓
Segmentation mask	×	×	✓	×	✓
Infrared rendering	×	×	✓	✓	✓
RGB rendering	✓	✓	×	×	✓
Reflective eye-wear	×	×	✓	×	✓
Lacrimal caruncle	×	×	×	×	✓
Variable eyelid position	×	×	✓	✓	✓
Real-time rendering	✓	×	×	×	×

Table 1: Comparison between existing synthetic rendering pipelines and datasets.

real-world eye imagery. By augmenting the synthetic data with a few real-world images, they observed an improvement in performance [25]. Together these studies suggest that the underlying distribution within existing synthetic datasets cannot capture the variability observed in real world eye imagery. While techniques such as few shot learning [25] and joint learning/un-learning [2] may help combat these issues, an inherently better training set distribution should aid in improving the performance of convolutional networks.

Here, we present a novel synthetic eye image generation platform and test its utility in the development of CNNs for semantic segmentation. This test involves using our framework to render three synthetic datasets: two that approximate the eye/camera/emitter position properties of publicly available datasets, one synthetic - NVGaze [18], and one of real eye imagery - OpenEDS [15]. The third dataset approximates the eye/camera/emitter properties of the Pupil Labs Core wearable eye tracker [16] and is referred to as S-General. Renderings which mimic NVGaze-synthetic and OpenEDS will be referred to as S-NVGaze and S-OpenEDS respectively. These datasets enable us to test the generalizability of our rendering pipeline. For example, if two CNNs trained on S-NVGaze and S-OpenEDS respectively exhibit little or no difference in performance when tested on an external image, we can conclude that properties differentiating S-NVgaze and S-OpenEDS (namely the camera orientation, and placement and number of emitters) do not contribute to the semantic understanding of different eye regions in the external image.

This work records the performance of two semantic segmentation models with varying complexity (SegNet [4] and RITnet [9]) trained on S-OpenEDS and S-NVgaze followed by testing on all available datasets (S-NVGaze, S-OpenEDS, S-General, NVGaze and OpenEDS). Network performance is used to identify the factors which limit our pipeline from generalizing across varying eye appearances and camera positions.

2 HEAD MODELS

Our rendering platform currently incorporates 24 head models with varying skin color, gender, and eye shape. Figure 1 provides several example near-eye renderings. Head models were purchased from an online repository¹. The associated textures contain 8K color maps captured using high-quality cameras. Eighteen models were selected to capture diversity (9 male, 9 female) in generating a training set, while the remaining 6 models (3 male and 3 female) were used to generate a testing set. To approximate the properties of human skin in the infrared domain, the red channel from the original diffuse texture map is incorporated for rendering purposes.

To overcome the challenge of controlling the placement of eyelashes relative to the eye-lid position, we replaced each of the model's original eyelashes with Blender's built-in hair particle editor which provides a plausible physical simulation of hair behavior. This is similar to the approach used by Swirski et al. [31]. We also replaced the basic 3D eyeball included with the 3D head models with our own customized 3D eyeball that provides greater control and more faithfully simulates the structure of real eyes.

3 EYE MODEL

Reconstructing all parameters that influence the imaging of a person's eye is a difficult task, and it is common to make simplifying assumptions regarding its structure. We used a modified Emsley-reduced optical model of the human eye [3, 11]. Table 2 summarizes the various basic physical properties. Modeling and rendering were accomplished using Blender-2.8.

Feature	Radius (mm)	Refractive index (n)
Cornea	7.8 mm	1.3375
Pupil	1-4 mm	×
Iris disc	6 mm	×
Eyeball sphere	12 mm	×

Table 2: Basic physical properties of our eye model. Radius and refractive index values courtesy of Dierkes et al. [11]

Furthermore, our eye model incorporates the following features:

Tear film: Similar to previous work [35], we designed a tear film on the outermost surface of the eyeball with glossy and transparent properties to produce plausible environmental reflections on the surface of the eye (see Figure 2).

Aspherical cornea: In contrast to previous work, we chose to render a physiologically accurate corneal bulge (see Figure 3). The corneal topography is modeled as a spheroid, $x^2 + y^2 + (1 + Q)z^2 - 2Rz = 0$ [12], where Q is the asphericity and R is the corneal radius of curvature. Research has shown that the human eye exhibits Q value of $\mu = -0.250$, $\sigma = 0.12$ [12]. Our corneal models incorporate three asphericity values, -0.130, -0.250 and -0.370, which were represented uniformly during rendering.

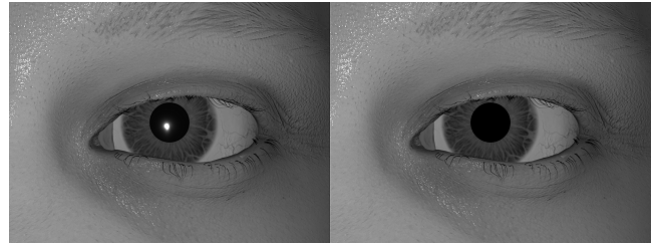


Figure 2: Comparison renderings to illustrate improvements offered by our model. With tear film (left). Without (right).

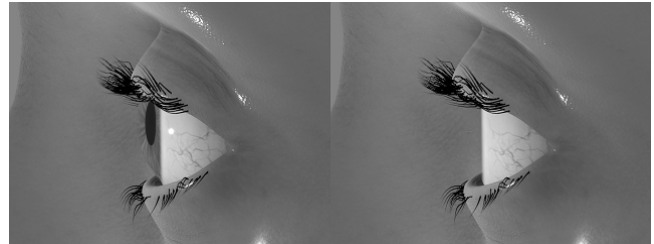


Figure 3: Comparison renderings to illustrate improvements offered by our model. With aspherical cornea (left). With no cornea (right).

Deformable eyelids: In order to avoid any visible gaps between the eyelids and the eyeball, the original 3D vertices in each eye socket were morphed to a snug fit around our custom eyeball. Using Blender's inbuilt wrapping function, we deformed the eyelid mesh to conform to the corneal contour below it. To mimic human behavior, the amount of eyelid closure was approximated by a linear function of eye rotation in the vertical axis (see Figure 4).

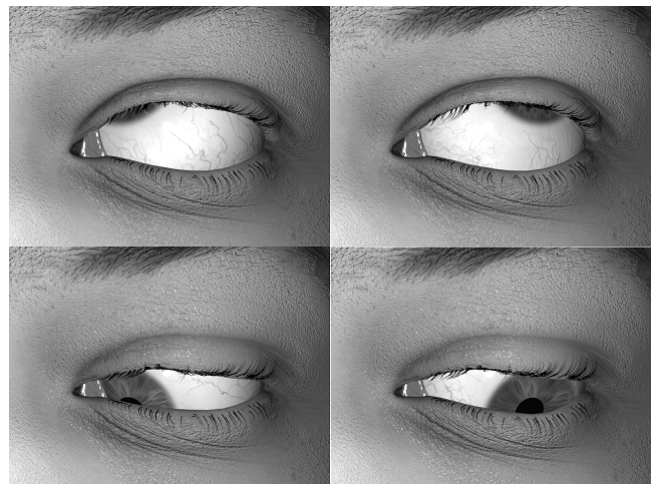


Figure 4: Renderings to illustrate improvements offered by our model. Eye lid deformation (shown at extreme gaze angles).

¹<https://www.3dscanstore.com/>

Pupil aperture: Previous datasets have modeled the pupil as an opaque black disc. The pupil in our eye model was accurately modeled as an aperture such that constriction or dilation of the pupil was accompanied by appropriate deformation of surrounding iris texture (see Figure 5). The pupil aperture opening was uniformly distributed between 1 mm to 4 mm in radius [11].

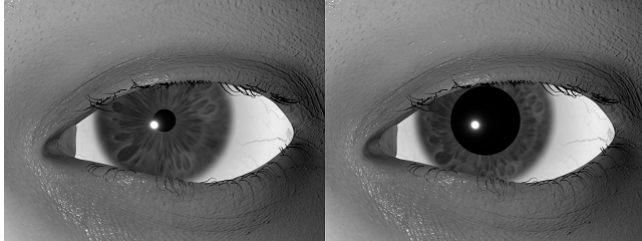


Figure 5: Renderings to illustrate improvements offered by our model. Variable size pupil aperture. 1 mm radius(left) to 3 mm radius(right).

Lacrimal caruncle: In contrast to previous works, we included the lacrimal caruncle, a small pink nodule positioned at the inner corner of the eye (see Figure 6). The lacrimal caruncle consists of skin, sebaceous glands, sweat glands, and hair follicles. Hence when generating the segmentation mask of the respective synthetic eye image, the lacrimal caruncle was considered to be part of the skin (see Figure 9) as opposed to OpenEDS [15], which segmented lacrimal caruncle as a part of sclera.

Bright pupil response: The bright pupil response occurs when a light source is within $\sim 2.25^\circ$ of separation from the imaging optical axis [24]. To simulate eye physiology, we added retroreflectivity to the retinal wall. Reflectivity increases as the angle of separation decreases following a Beckmann distribution (see Figure 7).

Environment mapping and reflective eye-wear: Following Wood et al. [35], we used 360° HDR images to simulate the reflections from the external environment. The environment texture is mapped onto a sphere with the eye model at its center. Each pixel intensity on the texture acts as a separate light source that illuminates the model. We used 25 HDR images obtained from an

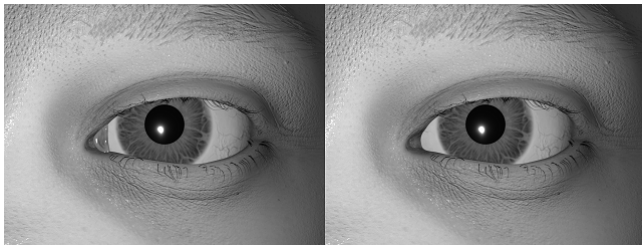


Figure 6: Comparison renderings to illustrate improvements offered by our model. With lacrimal caruncle (left). Without (right).

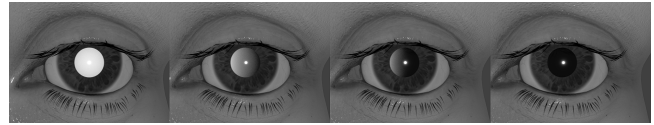


Figure 7: Renderings to illustrate improvements offered by our model. Bright pupil effect at varying degrees of angular separation between the imaging optical axis and the light source. From left to right: 0° , 1.16° , 1.51° , 2.25° .



Figure 8: Renderings with (left) and without (middle) glasses. Corresponding HDR environment map (right).

online repository.² Of these, nine were indoor, and 16 were outdoor scenes (see Supplementary Material). The pixel intensity of the environment texture was varied between $\pm 50\%$ of its original value. Textures were chosen at random, and their global intensity scaled to ensure equal proportions of dark, well lit, and saturated imagery. The environment map was rotated up to 360° along the y-axis and up to $\pm 60^\circ$ on the x and z-axis to induce a unique reflection pattern on the model for every rendered image. Figure 8 shows examples of environment mapping with and without reflective eye-wear.

Iris and sclera textures. Our rendering platform currently incorporates 9 infrared (IR) textures of the iris 7 obtained using IR photography of the human eye (courtesy of John Daugman [10]) and 2 artificial renderings previously used by Swirski et al. [30]. Note that among the 7 photographed textures of the iris, parts may be occluded due to eye lashes, eye lid position, or by reflections. In order to remove these artifacts, the images were manually edited using Photoshop. The texture for the sclera was purchased from an online repository³. Since, we only had access to one sclera texture and 9 iris textures, a random rotation between 0° and 360° was applied to the sclera and iris textures to increase variability in the rendered eye images.

4 RENDERED DATASETS

Three new datasets were rendered for use in the training of multiple independent (CNNs) for the semantic segmentation of eye features, and to test the ability for these CNNs to generalize across datasets collected using different configurations of the eye, camera, and infrared emitter(s). Two of the new datasets, *S-NVGaze* (see Figure 11) and *S-OpenEDS* (see Figure 10), are synthetic renderings intended to mimic the synthetic NVGaze [18] and real OpenEDS [15] datasets.

²<https://hdrihaven.com/>

³<https://www.cgtrader.com/>

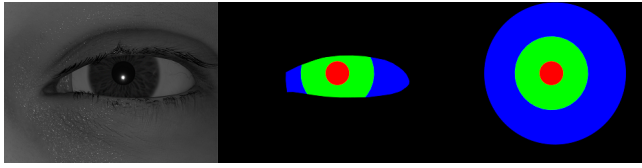


Figure 9: Sample synthetic image along with ground truth mask of pupil (red), iris (green), and sclera (blue) with and without skin.

The third dataset, *S-General* (see Figure 12) reflects a wide distribution of possible camera positions and orientations in the Pupil Labs Core mobile eye tracker. Each new dataset includes 51,600 path-traced images rendered using Blender’s Cycles rendering engine for a total of 154,800 images.

Eivazi et al. [13] augmented a dataset of real eye images by recording scene reflections off the anterior side of black coated glasses and superimposing them on the real eye imagery. To achieve similar reflections, we incorporate a 3 mm thick eyeglasses with black frames. Half the images in each dataset were rendered with eyeglasses.

Eye pose was uniformly distributed within $\pm 30^\circ$ in both azimuth and elevation. For each rendered image in the dataset, we generated ground truth masks of the sclera, iris, and pupil with and without the skin (see Figure 9) to facilitate evaluation of new and existing eye-tracking algorithms. We record additional metadata, including the 2D and 3D center of various eye features relative to the camera, as well as eye pose in degrees and the eye camera intrinsic matrix. A comprehensive list of the properties of the various datasets is provided in Table 3.

4.1 S-OpenEDS

OpenEDS is a dataset containing 12,759 off-axis images of real eyes that were captured with IR eye cameras positioned within a head mounted display [15]. To mimic the appearance of this dataset, we approximate eye camera orientation by overlaying and comparing segmentation masks. In order to approximate the lighting conditions of the OpenEDS dataset, 16 point-sources were arranged near the virtual eye camera in a circular pattern. Blender’s native compositor was used to imitate the resulting reflection pattern. The camera position is uniformly shifted ± 5 mm in the horizontal axis and vertical axis (see Figure 13) to simulate slippage of the HMD. The camera was rotated -10° along the elevation and the distance was uniformly varied from 3.5 cm to 4.5 cm from the tip of the eye based on empirical observations. Figure 10 shows side-by-side comparisons of images from OpenEDS and S-OpenEDS.

4.2 S-NVGaze

The NVGaze dataset contains 2M synthetic eye images generated using an on-axis camera configuration. For S-NVGaze, we rendered images at a resolution of 640 x 480 pixels with 200 rays per pixel. Similar to S-OpenEDS, we placed the camera in front of the eyes within an empirically derived distance of 3.5 cm to 4.5 cm from the tip of the eye. Eye camera position was varied ± 5 mm along

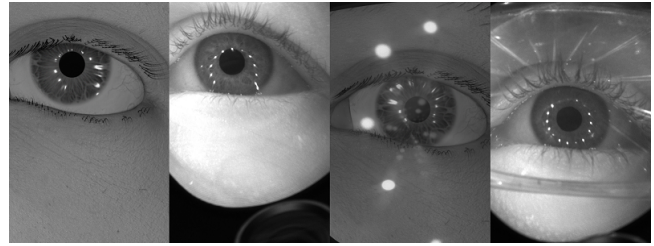


Figure 10: Comparison of images from S-OpenEDS (odd columns) with corresponding images from OpenEDS (even columns).

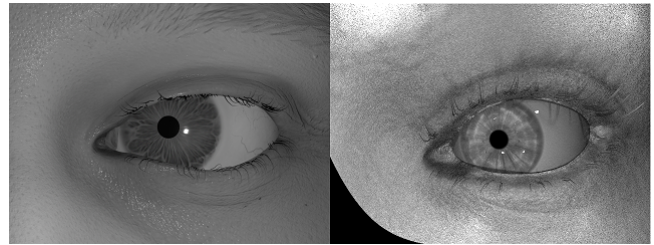


Figure 11: Comparison of image from S-NVGaze (left) with corresponding image from NVGaze (right).

the vertical and horizontal axes (see Figure 13) to match the simulated headgear slippage conditions observed in the NVGaze dataset. One point light source was placed near to the camera. Figure 11 shows a side-by-side comparison of an image from NVGaze with the corresponding image from S-NVGaze.

4.3 S-General

This dataset approximates the conditions imposed by the Pupil Labs Core mobile eye tracker. The camera position was uniformly distributed within an eye-centered spherical manifold subtending -20° to 60° along the azimuth and -20° to 40° in elevation (see Figure 13), which encompasses the range of camera positions afforded by the Pupil Labs Core mobile eye tracker. A smaller jitter of ± 1 mm in the vertical and horizontal plane is added to account for possible variation due to eye tracker slippage. Figure 12 shows example images of a fixed gaze with varying camera positions from the S-General dataset.

5 MODEL ARCHITECTURE

Two architectures were used when testing the ability for models to generalize across datasets collected using differing configurations of the eye, camera, and emitter(s): RITnet [9] (0.25M parameters) and SegNet [4] (24.9M parameters).

Dataset: Each dataset (S-OpenEDS, S-NVGaze, and S-General) consists of 39600 training images (36000 open eye cases, 1800 random eyelid position cases ranging from 80% to <100% closure and 1800 completely closed eye cases) of 18 head models and 12000

Dataset	Number Images	Resolution	Number of Subjects	Camera distance	Number of emitters
NVGaze	2M	1280 x 960	10 (5)	×	4
S-NVGaze (ours)	51,600	640 x 480	24 (12)	3.5 cm to 4.5 cm	1
OpenEDS	12,759	400 x 640	152 (82)	×	16*
S-OpenEDS (ours)	51,600	400 x 640	24 (12)	3.5 cm to 4.5 cm	16
S-General (ours)	51,600	640 x 480	24 (12)	2.5 cm to 4.5 cm	1

Table 3: Comparison of the image properties and camera setting used in NVGaze, S-NVGaze, OpenEDS, S-OpenEDS, S-General. The × symbol denotes a property that was either not reported, or not applicable. () indicated the number of female subjects. *Count based on number of corneal reflections.

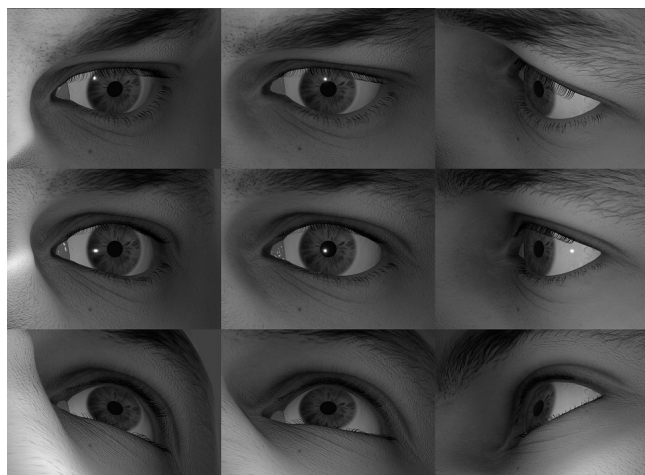


Figure 12: Sample images form S-General showing eye with fixed gaze and varying camera position. The camera position at -20°, 0°, 60° (left to right) in azimuthal plane and -20°, 0°, 40° in elevation plane (top to bottom).

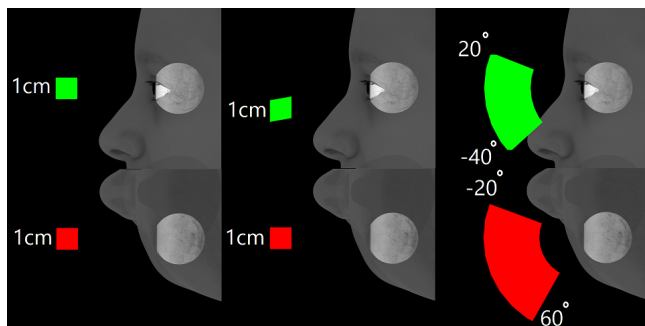


Figure 13: Camera positions used for S-NVGaze (left column), S-OpenEDS (middle column), and S-General (right column). Side-view (top). Top-view (bottom).

testing images of 6 different head models. Each training set is further divided into a 80-20 training/validation stratified split based on binned pupil center locations of each image.

To derive conclusions about varying eye camera poses and domain generalizability, each of the previously mentioned neural

network architectures (RITnet and SegNet), are trained under three different configurations: a) training with S-NVGaze, b) training with S-OpenEDS, and c) training with a combination of randomly selected S-NVGaze and S-OpenEDS images (50% each). A subset of images was set aside for model testing, including the entirety of the S-General dataset, 1500 random images extracted from each head model of the NVGaze dataset (60k images), and 2392 images present in the official OpenEDS validation set.

Training: We trained our models using the Adam optimizer [19] with a learning rate of $5e^{-4}$ for 40 epochs. We reduced the learning rate by a factor of 10 when the validation loss plateaued for more than 5 epochs. Both models are trained using the loss function strategy proposed in RITnet [9]. This strategy involves using a weighted combination of four loss functions:

- cross-entropy loss \mathcal{L}_{CEL}
- generalized dice loss [29] \mathcal{L}_{GDL}
- boundary aware loss \mathcal{L}_{BAL}
- surface loss [17] \mathcal{L}_{SL}

The total loss \mathcal{L} is given by a weighted combination of these losses as $\mathcal{L} = \mathcal{L}_{CEL}(\lambda_1 + \lambda_2 \mathcal{L}_{BAL}) + \lambda_3 \mathcal{L}_{GDL} + \lambda_4 \mathcal{L}_{SL}$. In our experiments, we used $\lambda_1 = 1$, $\lambda_2 = 20$, $\lambda_3 = (1 \text{ fit! } \alpha)$ and $\lambda_4 = \alpha$, where $\alpha = \text{epoch}/125$.

Image Augmentation: Image augmentation aids in broadening the statistical distribution of information content and combats overfitting [13]. Previous efforts [9, 27] have shown that data augmentation on eye images improves the performance of convolutional networks under naturalistic conditions such as varying contrast, eye makeup, eyeglasses, multiple reflections and image distortions. In this work, we utilize the following image augmentation schemes:

- (1) Since our work contains left-eye images exclusively, images were flipped about the vertical axis to simulate right eye conditions
- (2) Image blurring using a Gaussian kernel (width = 7 pixels, $\sigma = 2 - 7$ pixels)
- (3) Thin lines drawn around a random center (120 ; x ; 280, 192 ; y ; 448) [9] to simulate glare on glasses
- (4) Gamma correction with one of the following random factors: 0.6, 0.8, 1.2, or 1.4
- (5) Intensity offset up to ± 25 levels)
- (6) Down-sampling followed by the addition of random Gaussian noise (mean=0, $\sigma = 2$ to 16 levels) and up-sampling by factor of 2-5
- (7) No augmentation

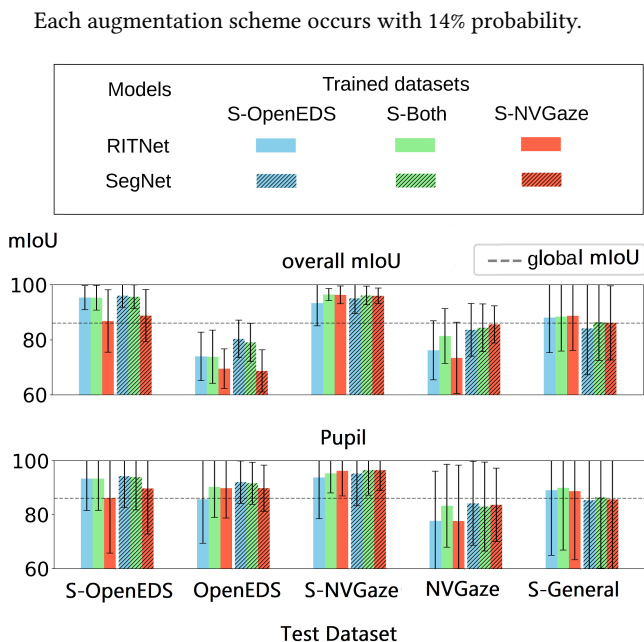


Figure 14: Results for overall mIoU and pupil-class mIoU. The horizontal axis consists of number of vertical blocks representing various test-dataset (S-OpenEDS, OpenEDS, S-NVGaze, NVGaze and S-General). Each block represents the performance of the particular dataset under various training conditions and models. Each block is further divided into unshaded and shaded blocks representing two model architectures, RITnet and SegNet respectively. Each of the unshaded/shaded block is further divided into three columns (S-OpenEDS (left), S-Both (middle) and S-NVGaze (right)). Each row indicate different cases (the overall mIoU and pupil class mIoU). The error bars show the standard deviation of the respective scores.

6 RESULTS AND DISCUSSION

Performance is evaluated using the *mean Intersection over Union (mIoU)* metric (in %) for both models in different test conditions for each class (pupil, iris, sclera, and background) and for all classes combined (which we refer to as the *overall mIoU*).

Results for *overall mIoU* and the pupil-class are summarized in Figure 14. Overall, the models performed quite well, with a *global mIoU* score (mean of all mIoU scores, indicated by the dotted line) of **86.06**. However, there is a large standard deviation in the overall mIoU (8.52) with scores ranging from 77.54- 94.59. For the pupil class, the standard deviation was 5.17 with a range of (84.09-94.43). Results for the other semantic classes (iris, sclera, and background) are included in the Supplementary Materials.

Below, we test several hypotheses related to model performance through targeted comparisons of training/testing data. For the sake of reference throughout the discussion section, and to better understand fluctuations in model performance, performance on these specific tests will be compared to the global mIoU.

TEST \ TRAIN	S-NVGaze	S-OpenEDS	S-NVGaze + S-OpenEDS
S-NVGaze	96.31/95.96	93.32/95.04	96.41/96.08
S-OpenEDS	86.81/88.75	95.30/95.99	95.28/95.62
S-General	88.71/86.11	88.06/84.11	88.40/86.37
NVGaze	73.38/85.57	76.17/83.61	81.36/84.36
OpenEDS	69.46/68.67	73.94/80.31	73.81/79.07

Table 4: Overall mIoU scores of the two models (RITnet / SegNet) when trained (listed on top row) on S-NVGaze, S-OpenEDS and both (S-NVGaze + S-OpenEDS) and tested (listed on the left column) on S-NVGaze, NVGaze, S-OpenEDS, OpenEDS, S-General. The best performing model is indicated using bold font. The highlighted colors are used as an easy references to explain the hypotheses discussed in Section 6. (This figure is best viewed in color.)

Do the CNNs generalize to head models not present during training? Tests reveal that models performed well above global mIoU when the CNNs were trained and tested using different head models, while keeping the manifold of camera positions/orientations constant across training and testing. This suggests that a CNN specifically trained for use with a particular eye tracker can generalize well to previously unseen faces that differ in both structure and appearance from the training set. Both S-OpenEDS and S-NVGaze achieved mIoU scores above 95 when tested on head models not used during training, as shown in Table 4 (highlighted in red).

How does the range of camera poses represented by the training dataset affect the ability to generalize to new camera poses? Our results demonstrate that the CNNs can generalize beyond the spatial area in which they were trained. This conclusion is supported by the fact that when the CNNs were tested on datasets in which the spatial distribution of camera positions/orientations were distinct from that represented by the training dataset, we observed performance at levels equal to or above the global mIoU. As shown in Table 4 (highlighted in green), when a model trained on S-OpenEDS was tested on S-NVGaze, the scores were 93.32 with RITnet and 95.04 with SegNet, and when trained on S-NVGaze and tested on S-OpenEDS, the scores were 86.81 with RITnet, 88.75 with SegNet.

Our models also demonstrated an ability to generalize across two distinct distributions of camera poses represented in the training set without a need to increase its size. There was no appreciable degradation of mIoU score when training using a dataset of the same size, with half of the images coming from S-OpenEDS and half coming from S-NVGaze, and testing with either S-OpenEDS or S-NVGaze (see Table 4, highlighted in red). Since there was no drop in performance relative to training and testing the datasets on subsets of their own imagery, we can conclude that the 39,600 image training dataset was a sufficiently dense sampling to account for simulated eye imagery taken from a camera position falling within the manifold spanning the regions represented in the first two columns presented in Figure 13.

Do the CNNs trained on one narrow spatial area generalize to a broader spatial area? Models are also able to perform at levels equal to or greater than the global mIoU when converged CNNs were tested against a synthetic dataset that represents a distribution of camera positions/orientations far larger than those present during training. When S-NVGaze (Figure 13, first column) was tested against S-General (Figure 13, third column), model performance reached an mIoU of 88.71 with RITnet, and 86.11 with SegNet. Similarly, when S-OpenEDS (Figure 13, middle column) was tested against S-General, model performance reached an mIoU of 88.06 with RITnet, and 84.11 with SegNet (see Table 4 highlighted in blue).

Do the CNNs trained on our synthetic imagery generalize to the datasets they were intended to mimic? We examine how the mIoU scores change when testing on our own synthetic data vs. when testing on the original datasets we are attempting to mimic. When trained on S-NVGaze and tested on S-NVGaze and NVGaze, we observe that the mIoU scores dropped from (S-NVGaze) 96.31→(NVGaze) 73.38 with RITnet and from (S-NVGaze) 95.96→(NVGaze) 85.57 for SegNet. Similarly, when trained on S-OpenEDS and tested on S-OpenEDS and OpenEDS, we observe that the mIoU scores dropped from (S-OpenEDS) 95.30→(OpenEDS) 73.94 for RITnet and (S-OpenEDS) 95.99→(OpenEDS) 80.31 for SegNet (see Table 4).

One might speculate that this drop in performance is due to a poor match between the manifold of camera positions represented in the training dataset and the testing dataset. However all the trained CNN models performed better when tested on S-General (see Table 4 highlighted in blue), which has a much different range of camera positions and poses compared to the training datasets, than when the models are tested on the datasets they are trying to mimic. This suggests that the drop in performance may not be due to a mismatch in camera positions/orientations, but to differences related to appearance and pixel level statistics. A likely reason for this could be poor identification of scleral regions (mIoU of 34.42 for RITnet, and 49.04 for SegNet when training and testing on S-OpenEDS and OpenEDS respectively and mIoU of 47.74 for RITNet and 75.60 for SegNet when training and testing on S-NVGaze and NVGaze respectively). Since we only have one scleral texture, the failure to generalize may be due to a lack of variability in appearance. The fact that we also consider the lacrimal caruncle as belonging to the background while OpenEDS annotations consider it an extension to scleral regions may also be a contributing factor.

Which model demonstrates better generalization? SegNet notably out performs RITnet when tested on OpenEDS ((RITnet) 73.94→(SegNet) 80.31) and NVGaze ((RITnet) 73.38→(SegNet) 85.57) after training on their synthetic counterparts. One cannot attribute these differences to loss functions, which were identical for all models presented here (note that these loss functions are different than those presented in [4]). The difference in performance may be due to the fact that RITNet has significantly fewer parameters (0.25M) compared to SegNet (24.9M).

Do the CNNs generalize across our synthetic datasets when considering only the pupil region? The pupil is comparatively easier to segment than other eye regions and also it is the primary

feature that is used to compute gaze direction in many current eye-trackers. We observe that pupil segmentation performance is indeed higher than the other eye regions (global mIoU for pupil/iris/sclera are 89.26/84.67/72.76 respectively). Furthermore, we observe that architectures trained on S-OpenEDS segment pupillary locations with higher accuracy on the S-NVGaze dataset (RITnet 93.76/SegNet 95.24) whereas the reverse (trained on S-NVGaze and tested on S-OpenEDS) is slightly degraded (RITnet 86.14 / SegNet 89.67). A potential reason for this behavior could be the difference in the number of glints present in S-OpenEDS (16) compared to S-NVGaze (1). Intuitively, if a network can accurately segment regions despite the presence of multiple glints, then that network would also perform well with fewer glints.

7 LIMITATIONS AND FUTURE WORK

The models tested here suffered moderate drops in performance when trained on our synthetic imagery, and then tested on the original datasets, which the synthetic imagery was intended to approximate. There are several ways in which one might improve the ability to generalize to the original datasets. We might see performance gains by more accurately or fully accounting for a wider range of complicating visual features. For example, although our datasets include near-eye images with eyeglasses, the simulated glasses currently only reflect incoming light, they did not refract light. Similarly, the presence of makeup, such as eye liner, eye shadow or mascara, which have been shown to interfere with many conventional algorithms for pupil detection and gaze estimation [15, 18], is not accounted for. Earlier works also do not address this.

Although the experimental design here was sufficient to test several hypotheses related to the utility of synthetic imagery, there are also several ways in which our methodology can be improved upon. Our test was limited to few segmentation models and fixed hyper-parameters. A detailed exploration of multiple segmentation models and hyper-parameter settings might improve the results. We use a traditional train/test paradigm to evaluate architecture performance, and this paradigm is particularly sensitive to image selection. We attempted to alleviate this limitation by opting for a stratified sampling approach based on binned pupil center locations. This approach might be improved upon through the use of techniques such as double cross-validation. The sensitivity of tests might also be improved through the use of other metrics such as deviation in pupil centers.

The tests also suggest that the gap between synthetic and real image distributions could be one of the reasons why the CNN models trained on synthetic images could not generalize well to the real world imagery. Recently, advances in generative adversarial networks (GANs) have shown great promise for improving style transfer from one image to another. GANs have been used to refine the appearance of images from the Unity Eyes synthetic dataset [28]. The improved appearance resulted in a smaller gaze error when compared to the unrefined images. Alternatively, it has been observed that the ability to generalize to real world imagery improves when a small number of hand-labelled real world eye images is included into the training set of synthetic eye imagery [18]. We plan to extend our rendering pipeline to leverage similar approaches.

In contrast to previous synthetic rendering pipelines that generate temporally non-contiguous frames, our framework can generate sequences of eye movements similar to those in real-world datasets like Gaze-in-Wild [20] and 360em [1]. We plan to explore if temporally contiguous eye images can be leveraged to improve the accuracy of gaze estimation algorithms.

Finally, although our work provides improvements to various eye features, it is still based on a simplified eye model and thus there is room for improvement. Recent work has attempted to extract accurate 3D information about various features of the eye, including the sclera and iris, from high resolution imagery [5–7]. We plan to explore if incorporating such information in our rendering pipeline can enhance the visual appearance of the synthetic eye imagery and improve performance of gaze estimation.

8 CONCLUSION

This paper presents a novel synthetic eye image generation platform that provides several improvements over existing work to support the development and evaluation of eye-tracking algorithms. This platform is used to render synthetic datasets, S-NVGaze and S-OpenEDS, reflecting the spatial arrangement of eye cameras in two publicly available datasets, NVGaze and OpenEDS. We demonstrate that networks trained solely with our synthetic images have the ability to generalize to unseen eye images. We also conclude that the spatial arrangement of eye camera does not contribute as heavily as the variation in eye image appearance. Images rendered from our dataset and converged models are made publicly available to aid researchers in developing novel gaze tracking solutions.

ACKNOWLEDGMENTS

We thank Dr. Errol Wood for providing the iris RGB textures from the Unity Eyes[34] and SynthEyes [35]. We thank Professor John Daugman[10] for providing infrared iris textures.

REFERENCES

- [1] Ioannis Agtzidis, Mikhail Startsev, and Michael Dorr. 2019. A Ground-Truth Data Set and a Classification Algorithm for Eye Movements in 360-degree Videos. (2019). <http://arxiv.org/abs/1903.06474>
- [2] Mohsan Alvi, Andrew Zisserman, and Christoffer Nellåker. 2019. Turning a blind eye: Explicit removal of biases and variation from deep neural network embeddings. *Lecture Notes in Computer Science (including subseries Lecture Notes in Artificial Intelligence and Lecture Notes in Bioinformatics)* 11129 LNCS (2019), 556–572. https://doi.org/10.1007/978-3-030-11009-3_34
- [3] David A. Atchison and Larry N. Thibos. 2016. Optical models of the human eye. *Clinical and Experimental Optometry* 99, 2 (2016), 99–106. <https://doi.org/10.1111/cxo.12352>
- [4] Vijay Badrinarayanan, Alex Kendall, and Roberto Cipolla. 2017. SegNet: A Deep Convolutional Encoder-Decoder Architecture for Image Segmentation. *IEEE Transactions on Pattern Analysis and Machine Intelligence* 39, 12 (11 2017), 2481–2495. <https://doi.org/10.1109/TPAMI.2016.2644615>
- [5] Pascal Bérard, Derek Bradley, Markus Gross, and Thabo Beeler. 2016. Lightweight eye capture using a parametric model. *ACM Transactions on Graphics (TOG)* 35, 4 (2016), 1–12.
- [6] Pascal Bérard, Derek Bradley, Markus Gross, and Thabo Beeler. 2019. Practical Person-Specific Eye Rigging. In *Computer Graphics Forum*, Vol. 38. Wiley Online Library, 441–454.
- [7] Pascal Bérard, Derek Bradley, Maurizio Nitti, Thabo Beeler, and Markus Gross. 2014. High-quality capture of eyes. *ACM Transactions on Graphics (TOG)* 33, 6 (2014), 1–12.
- [8] Martin Böhme, Michael Dorr, Mathis Graw, Thomas Martinetz, and Erhardt Barth. 2008. A software framework for simulating eye trackers. *Eye Tracking Research and Applications Symposium (ETRA)* 1, 212 (2008), 251–258. <https://doi.org/10.1145/1344471.1344529>
- [9] Aayush K. Chaudhary, Rakshit Kothari, Manoj Acharya, Shusil Dangi, Nitinraj Nair, Reynold Bailey, Christopher Kanan, Gabriel Diaz, and Jeff B. Pelz. 2019. RITnet: Real-time Semantic Segmentation of the Eye for Gaze Tracking. (2019), 1–5. <http://arxiv.org/abs/1910.00694>
- [10] John Daugman. 2009. How Iris Recognition Works. *The Essential Guide to Image Processing* 14, 1 (2009), 715–739. <https://doi.org/10.1016/B978-0-12-374457-9.00025-1>
- [11] Kai Dierkes, Moritz Kassner, and Andreas Bulling. 2018. A novel approach to single camera, glint-free 3D eye model fitting including corneal refraction. *Eye Tracking Research and Applications Symposium (ETRA)* June (2018). <https://doi.org/10.1145/3204493.3204525>
- [12] Georges M. Durr, Edouard Auvinet, Jeb Ong, Jean Meunier, and Isabelle Brunette. 2015. Corneal Shape, Volume, and Interocular Symmetry: Parameters to Optimize the Design of Biosynthetic Corneal Substitutes. *Investigative Ophthalmology & Visual Science* 56, 8 (7 2015), 4275. <https://doi.org/10.1167/iovs.15-16710>
- [13] Shaharam Eivazi, Thiago Santini, Alireza Keshavarzi, Thomas Kübler, and Andrea Mazzei. 2019. Improving real-time CNN-based pupil detection through domain-specific data augmentation. In *Proceedings of the 11th ACM Symposium on Eye Tracking Research & Applications - ETRA '19*. ACM Press, New York, New York, USA, 1–6. <https://doi.org/10.1145/3314111.3319914>
- [14] Wolfgang Fuhl, Thiago Santini, Gjergji Kasneci, Wolfgang Rosenstiel, and Enkelelda Kasneci. 2017. PupilNet v2.0: Convolutional Neural Networks for CPU based real time Robust Pupil Detection. (10 2017). <http://arxiv.org/abs/1711.00112>
- [15] Stephan J. Garbin, Yiru Shen, Immo Schuetz, Robert Cavin, Gregory Hughes, and Sachin S. Talathi. 2019. OpenEDS: Open Eye Dataset. (4 2019). <http://arxiv.org/abs/1905.03702>
- [16] Moritz Kassner, William Patera, and Andreas Bulling. 2014. Pupil: An open source platform for pervasive eye tracking and mobile gaze-based interaction. *UbiComp 2014 - Adjunct Proceedings of the 2014 ACM International Joint Conference on Pervasive and Ubiquitous Computing* (2014), 1151–1160. <https://doi.org/10.1145/2638728.2641695>
- [17] Hoel Kervadec, Jihene Bouchtiba, Christian Desrosiers, ftric Granger, Jose Dolz, and Ismail Ben Ayed. 2018. Boundary loss for highly unbalanced segmentation. <http://arxiv.org/abs/1812.07032>
- [18] Joohwan Kim, Michael Stengel, Alexander Majercik, Shalini De Mello, David Dunn, Samuli Laine, Morgan McGuire, and David Luebke. 2019. NVGaze: An anatomically-informed dataset for low-latency, near-eye gaze estimation. *Conference on Human Factors in Computing Systems - Proceedings* 12 (2019), 1–12. <https://doi.org/10.1145/3290605.3300780>
- [19] Diederik P. Kingma and Jimmy Ba. 2014. Adam: A Method for Stochastic Optimization. *AIP Conference Proceedings* 1631, 2 (12 2014), 58–62. <https://doi.org/10.1016/j.jneumeth.2005.04.009>
- [20] Rakshit Kothari, Zhizhuo Yang, Christopher Kanan, Reynold Bailey, Jeff B. Pelz, and Gabriel J. Diaz. 2020. Gaze-in-wild: A dataset for studying eye and head coordination in everyday activities. *Scientific Reports* (2020), 1–23. <https://doi.org/10.1038/s41598-020-59251-5>
- [21] Erik Lindén, Jonas Sjöstrand, and Alexandre Proutiere. 2018. Learning to Personalize in Appearance-Based Gaze Tracking. (7 2018). <http://arxiv.org/abs/1807>

00664

- [22] Carlos H. Morimoto and Marcio R.M. Mimica. 2005. Eye gaze tracking techniques for interactive applications. *Computer Vision and Image Understanding* 98, 1 (2005), 4–24. <https://doi.org/10.1016/j.cviu.2004.07.010>
- [23] Alejandro Newell, Kaiyu Yang, and Jia Deng. 2016. Stacked hourglass networks for human pose estimation. In *Lecture Notes in Computer Science (including subseries Lecture Notes in Artificial Intelligence and Lecture Notes in Bioinformatics)*. https://doi.org/10.1007/978-3-319-46484-8_{_}29
- [24] Karlene Nguyen, Cindy Wagner, David Koons, and Myron Flickner. 2002. Differences in the infrared bright pupil response of human eyes. *Eye Tracking Research and Applications Symposium (ETRA)* (2002), 133–138. <https://doi.org/10.1145/507097.507099>
- [25] Seonwook Park, Shalini De Mello, Pavlo Molchanov, Umar Iqbal, Otmar Hilliges, and Jan Kautz. 2019. Few-shot Adaptive Gaze Estimation. (5 2019). <http://arxiv.org/abs/1905.01941>
- [26] Seonwook Park, Adrian Spurr, and Otmar Hilliges. 2018. Deep Pictorial Gaze Estimation. Vol. 11217 LNCS. 741–757. https://doi.org/10.1007/978-3-030-01261-8_{_}44
- [27] Seonwook Park, Xucong Zhang, Andreas Bulling, and Otmar Hilliges. 2018. Learning to find eye region landmarks for remote gaze estimation in unconstrained settings. In *Eye Tracking Research and Applications Symposium (ETRA)*. ACM Press, New York, New York, USA, 1–10. <https://doi.org/10.1145/3204493.3204545>
- [28] Ashish Shrivastava, Tomas Pfister, Oncel Tuzel, Josh Susskind, Wenda Wang, and Russ Webb. 2017. Learning from simulated and unsupervised images through adversarial training. *Proceedings - 30th IEEE Conference on Computer Vision and Pattern Recognition, CVPR 2017* 2017-Janua (2017), 2242–2251. <https://doi.org/10.1109/CVPR.2017.241>
- [29] Carole H. Sudre, Wenqi Li, Tom Vercauteren, Sbastien Ourselin, and M. Jorge Cardoso. 2017. Generalised Dice overlap as a deep learning loss function for highly unbalanced segmentations. 10553 LNCS (7 2017), 240–248. https://doi.org/10.1007/978-3-319-67558-9_{_}28
- [30] Lech Świrski. 2015. Gaze estimation on glasses-based stereoscopic displays. August (2015).
- [31] Lech Świrski and Neil Dodgson. 2014. Rendering synthetic ground truth images for eye tracker evaluation. In *Eye Tracking Research and Applications Symposium (ETRA)*. 219–222. <https://doi.org/10.1145/2578153.2578188>
- [32] Lech Świrski and Neil A. Dodgson. 2013. A fully-automatic, temporal approach to single camera, glint-free 3D eye model fitting. *Pervasive Eye Tracking and Mobile Eye-Based Interaction (PETMEI)* (2013).
- [33] F. J. Vera-Olmos, E. Pardo, H. Melero, and N. Malpica. 2018. DeepEye: Deep convolutional network for pupil detection in real environments. *Integrated Computer-Aided Engineering* 26, 1 (2018), 85–95. <https://doi.org/10.3233/ICA-180584>
- [34] Erroll Wood, Tadas Baltruaitis, Xucong Zhang, Yusuke Sugano, Peter Robinson, and Andreas Bulling. 2015. Rendering of eyes for eye-shape registration and gaze estimation. In *Proceedings of the IEEE International Conference on Computer Vision*, Vol. 2015 Inter. IEEE, New York, NY, 3756–3764. <https://doi.org/10.1109/ICCV.2015.428>
- [35] Erroll Wood, Tadas Baltrušaitis, Louis Philippe Morency, Peter Robinson, and Andreas Bulling. 2016. Learning an appearance-based gaze estimator from one million synthesised images. *Eye Tracking Research and Applications Symposium (ETRA)* 14 (2016), 131–138. <https://doi.org/10.1145/2857491.2857492>
- [36] Yuk Hoi Yiu, Moustafa Aboulatta, Theresa Raiser, Leoni Ophey, Virginia L. Flanagan, Peter zu Eulenburg, and Seyed Ahmad Ahmadi. 2019. DeepVOG: Open-source pupil segmentation and gaze estimation in neuroscience using deep learning. *Journal of Neuroscience Methods* 324 (2019), 108307. <https://doi.org/10.1016/j.jneumeth.2019.05.016>
- [37] Xucong Zhang, Yusuke Sugano, Mario Fritz, and Andreas Bulling. 2015. Appearance-based gaze estimation in the wild. *Proceedings of the IEEE Computer Society Conference on Computer Vision and Pattern Recognition 07-12-June* (2015), 4511–4520. <https://doi.org/10.1109/CVPR.2015.7299081>